FUDMA Journal of Sciences (FJS)
ISSN online: 2616-1370
ISSN print: 2645 - 2944
Vol. 10 No. 6, March, 2026, pp 321 – 333
DOI: https://doi.org/10.33003/fjs-2026-1006-4907

MOLECULAR INSIGHTS INTO THE ADSORPTION BEHAVIOUR OF QUINOLINE-BASED SCHIFF BASE CORROSION INHIBITORS ON AL (111) SURFACE: A DFT AND MONTE CARLO STUDY

***[1]Abosede Adejoke Badeji, [2]Segun D. Oladipo, [3]Fulufhelo Tshikhudo and [4]Gideon A. Okon**

[1] Department of Chemical Sciences, Tai Solarin Federal University of Education, Ijebu Ode, Ogun State, Nigeria
[2] Department of Chemical Sciences, Olabisi Onabanjo University, Ago-Iwoye, Nigeria
[3] Department of Chemistry, School of Natural and Mathematical Sciences, Faculty of Science, Engineering and Agriculture, University of Venda, Private Bag X5050, Thohoyandou 0950, South Africa
[4]Department of Chemical Sciences, Clifford University, Owerintta, Nigeria.

*Corresponding authors' email: ogunlanaaa@tasued.edu.ng
https://orcid.org/0000-0002-9952-4618

ABSTRACT

The corrosion of aluminum in acidic environments poses significant challenges for industrial applications, necessitating the development of efficient corrosion inhibitors. In this study, the inhibition potential of two quinoline-based Schiff base derivatives, (E)-N-(4-fluorophenyl)-1-(quinolin-2-yl)methanimine (**B-Q4**) and (E)-N-(3-chloro-4-fluorophenyl)-1-(quinolin-2-yl)methanimine (**B-Q5**) , on the Al(111) surface in acidic medium, was investigated using density functional theory (DFT) calculations and Monte Carlo (MC) simulations. Quantum chemical calculations reveal strong intramolecular charge transfer and significant π-electron delocalization, which enhance the electron-donating ability of both inhibitors. NBO analysis shows high stabilization energies with π→ π* interactions and NCI and QTAIM analyses show that adsorption is dominated by weak dispersive interactions. Computational adsorption studies indicate that both inhibitors spontaneously react with the aluminum surface and that **B-Q4** exhibits more negative adsorption energies (stronger adsorption) at the DFT level. Monte Carlo simulations also indicate strong adsorption in a simulated acidic environment, with protonated species showing enhanced interaction due to electrostatic effects. The inhibitors adopt near-parallel orientations on the Al(111) surface, maximizing surface coverage and promoting the formation of a protective barrier. Overall, the results suggest that both compounds are effective corrosion inhibitors as DFT calculations in vacuum indicate stronger intrinsic adsorption for neutral **B-Q4**, while Monte Carlo simulations under acidic solvated conditions show that protonated **B-Q5H** exhibits superior adsorption due to enhanced electrostatic interactions. These complementary findings are consistent within their respective computational frameworks and collectively confirm the inhibition potential of both compounds.

Keywords: Corrosion Inhibitors, Aluminum (Al (111)) Surface, DFT, Monte Carlo Simulation, Adsorption Behavior

INTRODUCTION

Corrosion is a costly problem that is prevalent worldwide in nearly every industry, particularly those involving metal structures and components. It is a natural process of converting refined metals to their more stable oxide form (Bender et al., 2022; Kania, 2023; Zehra et al., 2022). A neutralization reaction between metals and acids is the most common form of corrosion, culminating in metal salts, among other compounds (Aljibori et al., 2023; Avdeev & Kuznetsov, 2022). Aluminium, one of the metals prone to corrosion, has been commonly used due to its excellent electrical conductivity, malleability, and resistance to atmospheric corrosion (Ikeuba et al., 2024). Despite its passive oxide layer offering some protection, aluminium remains susceptible to corrosion under aggressive environments such as acidic media, particularly hydrochloric acid (HCl), which can lead to significant material degradation. Birbilis and Hinton emphasized the growing application of aluminium and its alloys in structural engineering due to their mechanical strength and sustainability advantages, but also highlighted corrosion as a limiting factor affecting durability and lifecycle performance (Birbilis & Hinton, 2011). This challenge becomes even more critical in emerging applications like lithium-ion batteries, where Gabryelczyk *et al*. showed that corrosion of aluminium current collectors under specific electrochemical conditions can impair battery efficiency and lifespan (Gabryelczyk et al., 2021). To mitigate these issues, substantial efforts have been directed toward corrosion protection strategies. Among the most promising approaches are corrosion inhibitors, particularly those derived from natural or environmentally benign sources (Ahmed et al., 2024; Aslam et al., 2022; Aydın, 2023; Xhanari et al., 2017). As reviewed by Xhanari et al., green inhibitors such as plant extracts, oils, and natural polymers have shown significant promise in protecting aluminium and its alloys in various corrosive environments, including acidic media (Xhanari et al., 2017). These inhibitors function by adsorbing onto the metal surface, forming a protective barrier that suppresses the corrosion reaction. Furthermore, recent investigations into aluminium matrix composites (AMCs) by Aydın underscore the influence of microstructural modifications on corrosion resistance, where the presence and nature of reinforcements significantly alter electrochemical behavior (Aydın, 2023).

Hydrochloric acid is widely used in industrial processes such as acid cleaning, pickling, and descaling, where aluminium components are often exposed to aggressive acidic conditions. Under such environments, the protective oxide film on aluminium is compromised, leading to accelerated corrosion (Pietschmann, 2023; Saravanan et al., 2021; Wang & Wang, 2025). Although numerous studies have been conducted on corrosion inhibition in acidic media, most of the research has centered around carbon steel/HCl systems, where a broad range of organic inhibitors, such as plant extracts, drugs, ionic liquids, and polymers, have shown significant efficacy (Chen et al., 2022; Shahini et al., 2021; Zamindar et al., 2024). However, fewer studies have addressed the inhibition of

aluminium corrosion in hydrochloric acid, which presents a distinct mechanism due to the amphoteric nature of aluminium and the instability of its oxide layer in acidic media. Recent work by Alqarni *et al.* has shown that expired drug compounds like Ticarcillin and Carbenicillin can serve as effective inhibitors for aluminium in 1 M HCl, achieving significant inhibition efficiency through physical adsorption and the formation of a protective layer obeying Langmuir isotherm behavior (Alqarni et al., 2022). Recent advances in computational approaches—particularly Monte Carlo (MC) simulations—have provided atomistic insights into the adsorption efficiency of inhibitors on various metal substrates. For instance, small peptides have demonstrated enhanced predicted inhibitory activity due to increased adsorption energies and stronger molecular interactions with Al(111) surfaces (Kasprzhitskii & Lazorenko, 2021). Similarly, Xu et al. employed a combined MC, molecular dynamics (MD), and quantum mechanical approach to show that arginine exhibited the strongest computed adsorption energy (−210.39 kcal/mol) among the tested amino acids on Al(111), correlating well with its predicted inhibition efficiency (Xu et al., 2022). Another study by Uzah *et al.* revealed that thiosemicarbazide derivatives exhibit favorable adsorption on both Al(111) and Cu(111) surfaces, supported by low energy gaps and strong electrostatic potential interactions (Uzah, 2024). Sithuba et al. further employed DFT and MC simulations to evaluate Helichrysum kraussii extract components as corrosion inhibitors on Al(111) in 1.0 M HCl, reporting spontaneous adsorption and strong surface affinity from computational results (Sithuba et al., 2024). Toghan et al. similarly applied DFT and MD simulations to investigate the anticorrosion performance of naturally occurring compounds on aluminium surfaces, demonstrating the utility of combined computational frameworks for predicting inhibitor behavior (Toghan et al., 2023). These studies collectively demonstrate that DFT and MC simulations are well-established tools for evaluating corrosion inhibitor performance on Al(111), providing a strong computational basis for the present work.

Despite these advances, detailed molecular-level insights into how inhibitors bearing different halogen substituents interact with the aluminium surface, and how protonation under acidic conditions alter adsorption behavior, remain limited for quinoline-based Schiff base compounds. To address this gap, the present study integrates DFT calculations with MC simulations to systematically investigate the predicted adsorption characteristics of two quinoline-based Schiff base derivatives synthesized by our group (Oladipo et al., 2025), namely *(E)-N-(4-fluorophenyl)-1-(quinolin-2-yl)methanimine* (**B-Q4**) and *(E)-N-(3-chloro-4-fluorophenyl)-1-(quinolin-2-yl)methanimine* (**B-Q5**), on the Al(111) surface. This combined computational approach provides detailed insight into the molecular-level interactions governing the predicted adsorption strength, orientation, and stability of the inhibitors on the aluminum substrate, offering a complementary perspective to experimental findings. The novelty of this work lies in three specific areas: (i) the systematic comparison of two quinoline-based Schiff base inhibitors differing in halogen substitution pattern, mono-fluorine (**B-Q4**) versus chloro-fluoro (**B-Q5**), enabling a direct assessment of how halogen identity and combination influence predicted adsorption behavior on Al(111); (ii) the explicit comparison of neutral and protonated inhibitor forms under realistic acidic solvated conditions in MC simulations, capturing the protonation-dependent adsorption behavior that is important under HCl environments; and (iii) the integration of NBO, NCI, and QTAIM analyses alongside periodic DFT adsorption calculations and MC simulations, providing a multi-level electronic and topological characterization of the inhibitor–surface interaction for this class of compounds on Al(111). It is important to note that this is a predictive computational study; experimental electrochemical validation through techniques such as potentiodynamic polarization and electrochemical impedance spectroscopy is planned as future work. Specifically, this study tests the hypothesis that halogen substitution pattern (mono-fluorine in **B-Q4** vs. chloro-fluoro in **B-Q5**) and protonation state significantly influence adsorption geometry, predicted binding strength, and surface coverage on Al(111) under simulated acidic conditions.

MATERIALS AND METHODS

Overview and Justification of the Dual DFT Approach

In this study, two complementary DFT strategies were employed, with each selected for different specific aspects of the investigation. All calculations of isolated molecules, such as geometry optimization, NBO analysis, NCI analysis and QTAIM analysis were performed using Gaussian 16 with 6-311++G(d,p) basis set and hybrid functional B3LYP. This is a good choice since hybrid functionals like B3LYP give very good electron density distribution, good molecular geometry, and good orbital energetics in the gas phase for organic molecules and are the standard used in the electronic structure analysis of isolated inhibitor molecules in the corrosion inhibition literature (Azeez et al., 2023; Bedair et al., 2022; Ibeji et al., 2024).

On the other hand, all periodic slab calculations for the Al(111) surface and inhibitor–surface adsorption systems were done using Material Studio 2020 with the DMol³ module, using the GGA-PBE functional and the DNP basis set. Once the system is extended to a real metal surface, periodic boundary conditions are necessary to provide accurate modeling of the system, and the DMol³ implementation is specifically designed and tested for periodic metal–organic systems. In particular, GGA-PBE was chosen over hybrid functionals for the slab calculations for two main reasons: first, the computational cost of hybrid functionals scales steeply with system size which renders this method impractical for periodic DFT calculations of metal surfaces and metal–organic adsorption systems at the scale of the supercell sizes used here (5×5×1 supercell with three layers); second, GGA-PBE is the most widely accepted standard functional for periodic DFT calculations of metal surfaces and metal–organic adsorption systems, and is well accepted and used to predict the adsorption geometry and interaction energies for the study of corrosion inhibitors on metallic substrates (Sithuba et al., 2024; Vernack et al., 2020). The combination of the two methods (hybrid DFT for molecular electronic properties, GGA-PBE periodic DFT for surface adsorption) is commonly used in the computational corrosion inhibition literature and has the advantage that the most suitable and computationally tested methods are used in each part of the study.

DFT Studies of Isolated Inhibitor Molecules

All quantum chemical calculations on isolated molecules were conducted using the Gaussian 16 software package (Frisch et al., 2016). Geometry optimizations followed by vibrational frequency analyses were performed at the B3LYP level of theory with the 6-311++G(d,p) basis set (Andersson & Uvdal, 2005; Odozi et al,. 2022; Zhang et al., 2010). This combination offers a reliable approach for evaluating the structural and electronic properties of organic molecules. Frequency calculations confirmed that all optimized structures were true minima, as evidenced by the absence of

imaginary frequencies. Visualization of optimized geometries was carried out using Chemcraft while GaussView 6.0 was employed for building input files and analyzing outputs (Andrienko, 2010; Dennington et al., 2023). To assess the intramolecular non-covalent interactions in the isolated inhibitor molecules, NCI and QTAIM analyses were carried out to characterize the nature of intramolecular non-covalent interactions (Bader, 1985; Zhan et al., 2022). NBO analysis was also performed to assess the intramolecular charge delocalization and intramolecular donor–acceptor stabilization energies (Reed et al., 1988). It is noteworthy that the NCI analysis presented in Section 3.3 is only applicable to the isolated inhibitor molecules, describing intramolecular interactions, and it is not applicable to the interactions of the inhibitor molecules with the surfaces, which is discussed separately by the periodic DFT adsorption calculations in Section 2.3.

Periodic DFT Adsorption studies

Al•inhibited Interactions Analysis

The adsorption behaviour of **B-Q4** and **B-Q5** on Al(111) surface was studied using the DMol³ module of Material Studio 2020 software, which is based on the double numerical basis set with polarization functions (DNP-3.5) (Sithuba et al., 2024; Vernack et al., 2020), using periodic DFT within the generalized gradient approximation (GGA) and the Perdew–Burke–Ernzerhof (PBE) functional. Polarization d-function was added to all non-hydrogen atoms, while polarization p-function was added to hydrogen atoms. Acceleration of the convergence of self-consistent field (SCF) as well as relativistic effects explored in balancing the computational efficiency together with calculation accuracy, were accounted by DFT semi-core pseudopotentials (DSPP). The molecular geometry optimization of the aqueous phase environment of the isolated inhibitor molecules was performed using the COSMO solvation model; however, it must be noted that the DFT adsorption energy calculations on the Al(111) slab were performed in the gas phase (vacuum) without explicit solvation. As a result, the adsorption energies in Table 3 (which would be described in the later part) are intrinsic adsorption energies of the inhibitor on the surface, and do not take into account competitive adsorption by solvent molecules, solvation stabilization of the inhibitor, or electrostatic screening of the surface by ions. The effects of solvation are explicitly captured in the Monte Carlo simulation section, as inhibitor molecules interact with the Al(111) surface with explicit water molecules, hydronium ions and chloride ions present in the Monte Carlo system. The DFT adsorption energies should therefore be considered as an indication of the intrinsic electronic affinity of each inhibitor to the Al(111) surface and the Monte Carlo energies are more representative of the adsorption in a simulated acidic aqueous environment.

The Al(111) slab surface was built with a 5×5×1 supercell with a vacuum thickness of 20.00 Å and with three layers, two of which were constrained, and the topmost layer of the Al(111) slab serving as a active surface for adsorption. The adsorption energy (E_{ads}) and binding energy ($E_{binding}$) of the inhibitors on Al(111) surface were calculated using equations 1 and 2, respectively (Sithuba et al., 2024; Toghan et al., 2023).

$$E_{ads} = E_{subsrate\cdots adsorbate} - (E_{adsorbate} + E_{substrate}) \quad (1)$$

$$E_{binding} = -E_{ads} \quad (2)$$

Where $E_{subsrate\cdots adsorbate}$ is the total energy of the adsorbed inhibitor on the Al(111) surface, $E_{substrate}$ is the total energy of the clean Al(111) surface, $E_{adsorbate}$ is the total energy of the isolated optimized inhibitor. More negative values of E_{ads} indicate stronger and more favorable adsorption. All DFT adsorption energy values reported in this work are gas-phase (vacuum) values.

Monte Carlo Simulation

To complement the DFT results and to capture the adsorption behavior of the inhibitors on an aluminum surface under realistic acidic conditions, Monte Carlo (MC) simulation approach as implemented in the Materials Studio package was employed (Meunier & Robertson, 2021). The Al(111) surface was selected because it is the most thermodynamically stable and densely packed crystallographic plane of aluminum and is therefore commonly exposed in corrosion environments, as widely reported in experimental and theoretical corrosion studies (Sithuba et al., 2024; Uzah, 2024). Prior to the adsorption simulations, the geometries of the inhibitor molecules, **B-Q4** and **B-Q5**, as well as the solvent species, were optimized using the Forcite module in Materials Studio. The Condensed-phase Optimized Molecular Potentials for Atomistic Simulation Studies (COMPASS) force field was employed for the optimization and subsequent simulations due to its proven reliability in accurately describing interactions in organic molecules and metal–organic systems. The aluminum substrate was modeled by cleaving the Al(111) crystallographic plane to form a slab consisting of six atomic layers, and a 5 × 5 supercell was constructed to provide sufficient surface area for adsorption and to minimize periodic boundary artifacts. The lattice parameters of the simulation cell were set to a = 28.634289 Å, b = 28.634289 Å, and c = 31.689900 Å, corresponding to a crystal thickness of 31.6899 Å. To avoid spurious interactions between periodic images along the surface normal, a vacuum slab of 20 Å was introduced in the z-direction. The Al(111) surface was kept rigid (frozen) during all MC simulations, as is standard practice for Adsorption Locator-based MC studies; this approximation is justified by the significantly stronger nature of Al–Al cohesive interactions relative to the inhibitor–Al physisorption interactions studied here.

To replicate an acidic aqueous corrosion environment, the simulation cell was solvated with 80 water (H_2O) molecules, 10 hydroxonium (H_3O^+) ions, and 10 chloride (Cl^-) ions to mimic the acidic chloride medium commonly employed in corrosion experiments. The inhibitor molecules (**B-Q4** and **B-Q5**) and their protonated form (**B-Q4H** and **B-Q5H**) were then placed above the Al(111) surface within the solvated simulation box and subjected to MC simulations using the Adsorption Locator module to identify the most energetically favorable adsorption configurations.

All simulations were run for 5 cycles with 50,000 MC steps per cycle, giving a total of 250,000 steps. Optimization of the geometry was done at each cycle using an energy convergence tolerance of 1.0×10^{-4} kcal/mol, a force convergence tolerance of 0.005 kcal/mol/Å, and a displacement convergence tolerance of 5.0×10^{-5} Å. with a maximum of 500 iterations per cycle. Temperature was controlled using the automated simulated annealing protocol, and the highest and lowest temperatures were 1.0×10^5 K and 100.0 K, respectively, allowing for a wide conformational sampling that leads to convergence of the energetically favorable adsorption configurations. The simulation was done under zero external pressure (0.0 GPa). The MC moves were sampled with equal probability for conformer, rotation, and translation steps (probability 0.32 each) and regrowth moves with lower probability of 0.03. The adsorption process was evaluated by analyzing the total adsorption energy, rigid adsorption energy, and deformation energy obtained from the simulation results. These parameters provide insight into the

interaction strength, adsorption stability, and surface affinity of **B-Q4** and **B-Q5** toward the aluminum surface under simulated acidic conditions. It is emphasized that the total adsorption energies given from the MC simulations are related to the total interaction energy of the complete simulation cell, including the Al(111) surface, the inhibitor and solvent molecules and the ions interacting with the Al(111) surface and that the total energy is therefore not directly comparable in magnitude to the per-molecule adsorption energies in the gas-phase.

RESULTS AND DISCUSSION

Geometry Optimization

In our previous report, we have described the optimized geometries of **B-Q4** and **B-Q5**. We revealed that there is close structural similarities in the two geometries and that halogen substitution (Cl) does not significantly alter the core geometry but may influence localized electronic distributions (Figure 1).

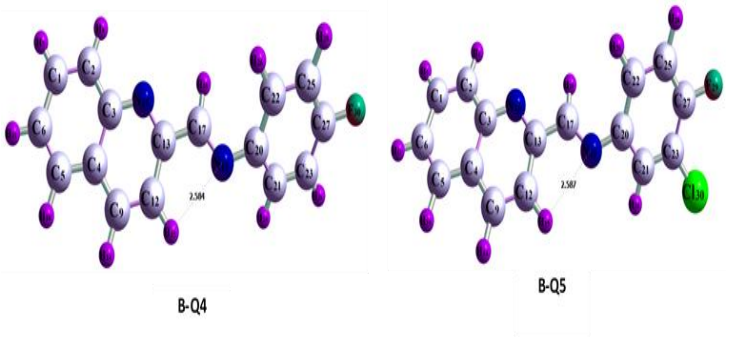

Figure 1: Geometry Plots of B-Q4 and B-Q5

NBO Analysis

The NBO analysis provides insight into the intramolecular charge delocalization and stabilizing interactions (electron-donating and electron-delocalization ability) of **B-Q4** and **B-Q5**, which are key features that determine their effectiveness as corrosion inhibitors. In corrosion inhibition, molecules with strong charge-transfer capability and extensive electron delocalization generally adsorb more effectively on a metal surface, thereby enhancing the formation of a stable protective film. The second-order perturbation energy ($E^{(2)}$) values measure the strength of donor–acceptor interactions between occupied (donor) and unoccupied (acceptor) orbitals. This reflects the molecular electronic stability and reactivity (Louis et al., 2021; Ma et al., 2023) and is calculated using equation 3.

$$E^{(2)} = \Delta E^2 ij = qi \frac{(Fi,j)^2}{(Ej-Ei)} \quad (3)$$

Where *qi* denotes the electron donor orbital occupancy, Ei and Ej stand for the orbital energies of the donor and acceptor orbitals.

The π→π* forward donations across the quinoline–imine–aryl framework are the dominant interactions in both inhibitors. The π(C9–C12)→π*(C13–N16) interaction (22.86 kcal/mol) is the largest stabilization energy in **B-Q4**, following closely by the π(C21–C23)→π*(C25–C27) (22.40 kcal/mol) and π(C13–N16)→π*(C3–C4) (20.08 kcal/mol) interactions, which indicate the extensive electron delocalization across the quinoline ring into the fluorobenzene fragment through the imine linkage of **B-Q4** (Table 1). Similarly, for **B-Q5**, the π(C9 – C12)→π*(C13 – N16) π-electron interaction is responsible for the maximum E(2) value of 23.02 kcal/mol, suggesting that the cross-conjugation is slightly stronger in the case of **B-Q5** than **B-Q4**. Further stabilization occurs through LP→π* and LP→σ* delocalizations, with the participation of the lone pairs on the heteroatoms, especially the N, F, and Cl atoms.

The active participation of the imine nitrogen in the electron redistribution is manifested in the similar $E^{(2)}$ values of 12.79 and 12.67 kcal/mol obtained for both inhibitors in the case of LP(1) N19→σ*(C17–H18). Electronic donation of the lone pair of electrons of fluorine to π*(C25–C27) in **B-Q4** (17.71 kcal/mol) and to π*(C25–C27) in **B-Q5** (18.38 kcal/mol) indicates that the fluorine atom provides a substantial contribution to the conjugation of the aryl ring and is not just a purely inductive substituent (Table 1). The relatively high stabilization energies and low donor-acceptor energy gaps observed for both molecules suggest strong orbital interactions and significant conjugation in their molecular structure, especially for **B-Q5** which has a LP(3) Cl30→π*(C21–C23) interaction, absent in **B-Q4**, due to the electron donating potential of the chlorine atom into the adjacent aromatic π system. This additional delocalization pathway, together with marginally more effective fluorine lone pair delocalization in **B-Q5**, leads to overall stronger lone-pair-assisted delocalization in **B-Q5** than in **B-Q4** and accounts for the differences in the adsorption behavior observed in the DFT and Monte Carlo studies. The overall NBO results indicate that both inhibitors have well spread-out π-electron systems, as well as several centers containing electron-rich heteroatoms, which are desirable for adsorption to the surface of the metal aluminum via donor–acceptor interactions.

Table 1: Natural Bond Orbital (NBO) Parameters of B-Q4 and B-Q5

Complexes	Donor (i)	Acceptor (j)	E^2 Kcal/mol	$E_{(j)}$-$E_{(i)}$	F(i,j) (a.u.)
B-Q4	π C13–N16	π * C3–C4	20.08	0.33	0.077
	π C9–C12	π * C13–N16	22.86	0.28	0.073
	π C21–C23	π * C25–C27	22.40	0.28	0.071
	LP(1) N19	σ * C17–H18	12.79	0.74	0.088
	LP(3) F30	π * C25–C27	17.71	0.43	0.085
	LP(1) N16	σ* C12–C13	10.72	0.87	0.087

Complexes	Donor (i)	Acceptor (j)	E^2 Kcal/mol	$E_{(j)}$-$E_{(i)}$	F(i,j) (a.u.)
B-Q5	π C9–C12	π * C13–N16	23.02	0.28	0.073
	π C13–N16	π * C3–C4	19.96	0.33	0.077
	π C20–C22	π * C21–C23	21.75	0.27	0.069
	LP(1) N19	σ* C17–H18	12.67	0.74	0.088
	LP(3) F29	π * C25–C27	18.38	0.43	0.086
	LP(3) Cl30	π * C21–C23	12.74	0.32	0.063

Non-Covalent Interaction (NCI) Analysis

Non-covalent interaction (NCI) analysis is a powerful visualization tool used to identify and characterize weak intermolecular and intramolecular interactions, including electrostatic interactions, π–π stacking, van der Waals forces, hydrogen bonding, steric repulsion, and hydrophobic effects (Lu, 2025). In contrast to covalent bonds, which involve the sharing of electron density between atoms, non-covalent interactions are comparatively weaker and originate from electrostatic attraction, dispersion forces, and polarization effects (Zhan et al., 2022). The quantum theory of atoms in molecules (QTAIM) developed by Bader is a rigorous theoretical approach to explaining chemical bonding and molecular structure through the topology of the electron density distribution (Bader, 1985). An important topological characteristic of QTAIM is the bond critical point (BCP), a saddle point of the electron density along the bond path where the gradient of the electron density, $\nabla\rho(r)$ is zero. The nature of interactions at BCPs is interpreted through several real-space descriptors. These are the electron density at the BCP ($\rho(r)$), the Laplacian of the electron density ($\nabla^2\rho(r)$), total energy density (H(r)), electron localization function (ELF), ellipticity (ε), and eigenvalues of the Hessian (λ_1, λ_2, λ_3) (Gervasio et al., 2004). Typically, larger values of $\rho(r)$ show that there are stronger bonding interactions and smaller values imply weaker or no covalent interactions. The Laplacian of the electron density ($\nabla^2\rho(r)$) represents the sum of all three eigenvalues ($\lambda_1 + \lambda_2 + \lambda_3$) calculated from the Hessian matrix. If $\nabla^2\rho(r)$ has a negative value, then there is an increase in electron density between interacting atomic nuclei, usually indicative of a covalent bond. Conversely, positive values represent loss of electron density between atomic nuclei, which is indicative of ionic, hydrogen-bonded or Van der Waal's forces (Badeji et al., 2025). Partially covalent interactions can exist if $\nabla^2\rho(r) > 0$, yet have a negative H(r). The total energy density H(r) is defined as the sum of both Lagrange's kinetic energy density G(r) and potential energy density V(r). Negative values of H(r) tend to be covalent interactions, which are stabilized by formation of bonds, and positive H(r) values are usually indicative of ionic interactions (Pal et al., 2022).

The NCI and QTAIM analyses carried out in this study were on the isolated inhibitor molecules **B-Q4** and **B-Q5** in the gas phase and hence, characterize the intramolecular non-covalent interactions only. They do not directly probe the bonding between the inhibitor and the Al(111) surface bonding and cannot determine the nature of the inhibitor–surface interaction. The NCI plots for **B-Q4** and **B-Q5** (Figure 2A) show a similar interaction pattern. NCI plots show a green isosurface corresponding to weak van der Waals attractions, or nearly neutral interactions, and a red isosurface corresponding to repulsive interactions that are caused by steric hindrance. Van der Waals interactions are depicted by green isosurface regions, and as they grow in volume and intensity in blue coloration, they show the formation of stronger attractive interactions such as hydrogen bond. In agreement with this, the green isosurfaces in **B-Q4** and **B-Q5** are spread between H-H atoms throughout the molecular structure, suggesting mostly weak van der Waals type interactions, while the red isosurfaces are concentrated around the aromatic ring and along the molecular backbone, corresponding to steric repulsion caused by electron cloud congestion in those areas (Galvez et al., 2025; Suvitha et al., 2019). These intramolecular interactions are weak individually but collectively important, as they contribute to the stabilization of the molecular structure and the conformational rigidity of the inhibitors, which affects the molecule's orientation during adsorption. Comparatively, **B-Q5** shows slightly more extended green regions across the aromatic framework, suggesting a marginally stronger dispersive interactions within the molecule. Both systems maintain slightly more localized interactions, particularly around the heteroatom N-H and halogen (Cl- and F-) linkages, which are the regions most likely to engage with the metal surface during adsorption.

The QTAIM molecular graphs (Figure 2B) illustrate orange dots as BCPs and yellow dots as ring critical points (RCPs), which are present throughout the molecular frameworks of both inhibitors, further confirming the intramolecular bonding topology of these conjugated systems. The identified BCPs and their topological parameters are given in Table 2. For **B-Q4**, BCPs are identified for F_{30}–C_{27}, N_{19}–C_{17}, N_{16}–C_3, and C_6–H_{11}, while for **B-Q5**, BCPs are found for N_{19}–C_{20}, C_{12}–C_9, F_{29}–C_{27}, and N_{16}–C_3. For all the BCPs reported here, the values of $\nabla^2\rho$ are negative and the values of H(r) are negative, which indicates that the intramolecular bond is predominantly shared-shell covalent. The highest electron densities along with the most negative H(r) values are found for N–C bonds, such as N_{19}–C_{17} with $\rho = 0.359$ and $H(r) = -0.476$ in **B-Q4** and N_{16}–C_3 with $\rho = 0.302$ and $H(r) = -0.312/-0.313$ in both inhibitors, which is indicative of strong covalent interactions centered on the electron-rich nitrogen atoms. The electron densities and H(r) values of the C–F bonds in both inhibitors, F_{30}–C_{27} in **B-Q4** ($\rho = 0.239$, $H(r) = -0.250$) and F_{29}–C_{27} in **B-Q5** ($\rho = 0.244$, $H(r) = -0.259$), are comparatively low, and are partly due to the more polar and partially ionic nature of the halogen–carbon bond compared to the N–C bond. The electron localization values (ELF) along these intramolecular bonds are also high, with values from 0.608 to 0.990, confirming the good electron localization along these bonds. Taken together, these QTAIM parameters indicate that electron density is significantly localized at the N and halogen atoms in both inhibitors, which correspond to the electron-donating sites in the molecular framework as suggested by the NBO donor–acceptor analysis.

It should be noted that no BCPs was reported between the Al(111) surface and the inhibitor molecules since QTAIM was not carried out on the Al(111)···inhibitor adsorption complex. These calculations can then not determine the absence of intermolecular Al–inhibitor BCPs.

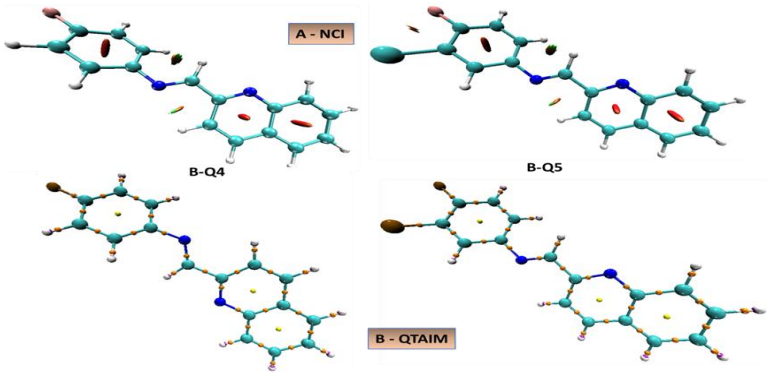

Figure 2: (A) The Isosurface Maps Of The Non-Covalent Interaction Analysis Of The Systems To Characterize The Nature Of Bonds Present Using The VMD Software(Humphrey Et Al., 1996), And **(B)** The QTAIM Molecular Graphs Of The Systems

Table 2: The Calculated Topological Parameters: Electron Density P(R), Laplacian Electron Density ∇^2(R), Lagrangian Kinetic Energy G(R), Potential Electron Energy Density V(R), Total Electron Energy Density H(R), Eigen Values (Λ1, Λ2, Λ3), And Ellipticity (Ɛ) Of The Studied Complexes At The Bond Critical Points (Bcps). All Values Are In A.U

Complexes	Bond	BCP	ρ(r)	G(r)	K(r)	V(r)	H(r)	$\nabla^2\rho^{(2)}$	ELF	λ_1	λ_2	λ_3
B-Q4	$F_{30} – C_{27}$	37	0.239	0.203	0.251	-0.453	-0.250	-0.191	0.630	-0.421	-0.386	0.616
	$N_{19} – C_{17}$	47	0.359	0.298	0.476	-0.774	-0.476	-0.715	0.753	-0.780	-0.734	0.799
	$N_{16} – C_3$	43	0.302	0.161	0.312	-0.473	-0.312	-0.605	0.854	-0.610	-0.588	0.592
	$C_6 – H_{11}$	54	0.275	0.343	0.248	-0.282	-0.248	-0.854	0.990	-0.784	-0.775	0.704
B-Q5	$N_{19} – C_{20}$	43	0.273	0.129	0.252	-0.380	-0.252	-0.491	0.867	-0.527	-0.514	0.549
	$C_{12} – C_9$	36	0.322	0.125	0.367	-0.493	-0.367	-0.967	0.923	-0.635	-0.545	0.214
	$F_{29} – C_{27}$	50	0.244	0.219	0.259	-0.479	-0.259	-0.160	0.608	-0.422	-0.393	0.655
	$N_{16} – C_3$	55	0.302	0.161	0.313	-0.474	-0.313	-0.606	0.854	-0.610	-0.588	0.592

With regard to charge analysis, it is mentioned in our previous study (Oladipo et al., 2025) that both **B-Q4** and **B-Q5** were synthesized and extensively characterized in terms of their electronic structure and biological activity. In that work, Mulliken charges of these two isolated inhibiors were calculated at the B3LYP/6-311++G(d,p) level of theory and both gas phase and aqueous. C4 was always found to be the most electropositive carbon atom in both inhibitors irrespective of the medium (gas or solvent phase) while C3 was always found to be the most electronegative carbon atom in both inhibitors implying its electron accepting capacity. The close proximity of C3 to the quinolinic nitrogen is attributed to its high electronegative value. The positive charges on all the hydrogen atoms were positive, with H15 being most electropositive in the gas phase, because of the weak intramolecular hydrogen bond with N16 (2.58 Å), while H28/H29 were most electropositive in the aqueous phase because of increased intramolecular hydrogen bond with F30 by solvation. The negative charge of the fluorine atom did not change in both inhibitors in any media, and the positive charge of the chlorine atom was present in **B-Q5** in all media. The nitrogen atoms were positively charged, with N19 being more electropositive than N16 in **B-Q4** because of the participation of N19 in the delocalization of the π-electron system of fluorobenzene. The overall charge distribution analysis reveals well-defined electron rich and electron deficient regions in the inhibitors, which are conducive to the electron deficient aluminium surface via donor–acceptor interactions, and the lack of large-scale charge reorganization is in agreement with adsorption of the inhibitors to the aluminium surface in the predominant physisorptive mode. Meanwhile, it should be noted that the charge analysis was not carried out between the inhibitors and the aluminum surface.

Adsorption Studies

Investigation of the Inhibition Potential of B-Q4 and B-Q5 against Aluminum

To understand the interaction between the inhibitors (**B-Q4** and **B-Q5)** and aluminum surfaces as well as identify the nature of bonding (physical or chemical) together with adsorption strength, we explored DFT for this study. The adsorption energies (ΔE_{ads}, kcal/mol), binding energies (ΔE_{bind}, kcal/mol), relative energies (ΔE_{bind}, kcal/mol), and bond distances (Å) between the Al surface and the **B-Q4** and **B-Q5** inhibitors were computed and presented in Table 3. These optimized inhibitor···Al structures are also illustrated in Figure 3 & 4 The various configurations of the inhibitor on the aluminum surface are denoted by alphabetic letters appended to the Al···inhibitor symbol. For example, the symbol (**B-Q4**···Al)-a represents one possible arrangement of the interaction between the aluminum surface and **B-Q4**, while (**B-Q4**···Al)-b denotes a different arrangement of the binding between the aluminum surface and the **B-Q4** inhibitor. In order to identify the most stable and preferred configurations of an inhibitor molecule on a metal surface the relative energies were calculated. Arrangements with relative energies below 4 kcal/mol are considered the most stable and favorable for inhibitor binding to the metal surface (Sithuba et al., 2024).

For **B-Q4**···Al, among the four possible arrangements, two configurations were identified as the most stable and preferred, with relative energies of 0 and 0.0107 kcal/mol and the nearest heteroatom bond distance of (Al···F) 2.256 Å, (Al···N) 2.464 Å, (Al···N) 2.477 Å, and (Al···N) 2.049 Å, (Al···N) 2.073 Å, respectively. The **B-Q4** inhibitor tends to adopt either a horizontal or perpendicular orientation when adsorbing onto the aluminum surface. The perpendicular orientation arises from the interaction between the aluminum

surface and the nitrogen atoms in **B-Q4**, forming Al···N bonds. In the case of **B-Q5**, all configurations exhibit relative energies below 1 kcal/mol, indicating that the **B-Q5** inhibitor can adopt any of the five arrangements when interacting with the aluminum surface with the bond distance ranging from 3.00 to 5.00 Å. **B-Q5** also exhibits two orientations, with the perpendicular configuration resulting from the fluorine atom forming an Al···F bond. Based on these observations, it can be concluded that horizontal orientations provide stronger interactions between inhibitor and metal surface and, therefore, offer better corrosion inhibition compared to perpendicular configurations (Figure 3 and Figure 4).

In **Table 3**, the adsorption energy for all the inhibitors is negative and this confirms the adsorption of the inhibitor molecules to be spontaneous (Kumar et al., 2024) on the energetic surface of the Al with the corresponding Miller index of (111). The negative adsorption energy for **B-Q4** is in the range of 6.6540 - 39.7314 kcal/mol for all the configurations while for **B-Q5**, it was within the range of 5.4228 – 9.1866 kcal/mol. The adsorption energies for (**B-Q4**···Al)-a and (**B-Q4**···Al)-b configurations are -39.7314 kcal/mol and -39.7207 kcal/mol respectively and these values are the highest among all configurations in this study. This suggests that **B-Q4** could inhibit corrosion on aluminum surface stronger than to **B-Q5** under gas-phase conditions. This difference is explained by the presence of one fluorine atom in **B-Q4**, which allows more localised and directional interaction between the inhibitor and the aluminum surface, while the additional chlorine atom in **B-Q5** causes some steric effects which partly hinder the contact between the inhibitor and the aluminum surface. As discussed earlier in section 2.3.1, these adsorption energies are intrinsic gas-phase values. Literature has reported that adsorption energies greater than −100 kcal/mol signify chemisorption and those with magnitude below −100 kcal/mol are associated with physisorption (Farag et al., 2024). The computed adsorption energies for **B-Q4** and **B-Q5** inhibitors are below -100 kcal/mol in magnitude, suggesting that their interaction with aluminum surface took place through physical adsorption (physisorption). This is further supported by the molecular electronic structure of the inhibitors, the dispersive intermolecular interactions revealed by NCI analysis and the electron density localization at nitrogen and halogen centers from NBO analysis, and the charge distribution reported by Oladipo et al. (2025), all of which indicate that both inhibitors possess the electronic character typical of physisorbing molecules, interacting with metal surfaces through weak, delocalized contacts rather than bond formation.

It is interesting to note however, that the perpendicular conformation (**B-Q4**···Al)-b (where ΔE = 0.0107 kcal/mol) has Al···N bond distances of 2.049 and 2.073 Å. These are close to the minimum reported for Al–N coordination interactions (~2.0–2.2 Å), indicating that the N atoms in **B-Q4** might participate in relatively close surface contacts in the perpendicular orientation. However, this is not a change from the physisorption as the adsorption energy is still significantly less than the chemisorption threshold, no bonding is suggested by the NBO or NCI analyses, and short heteroatom–surface distances have been reported in the literature for N-containing physisorbing inhibitors on Al(111) (Sithuba et al., 2024; Uzah, 2024). In contrast, the most stable horizontal configuration (**B-Q4**···Al)-a gives distances of 2.256 – 2.477 Å for Al···F and Al···N, which are unambiguously in the physisorptive range, as well as all **B-Q5** configurations (3.00 – 5.00 Å). The overall physisorption assignment for both inhibitors is, therefore, strong, and it is seen that the closest contacts between heteroatoms and the surface for the inhibitors occurs in the perpendicular orientation for **B-Q4**.

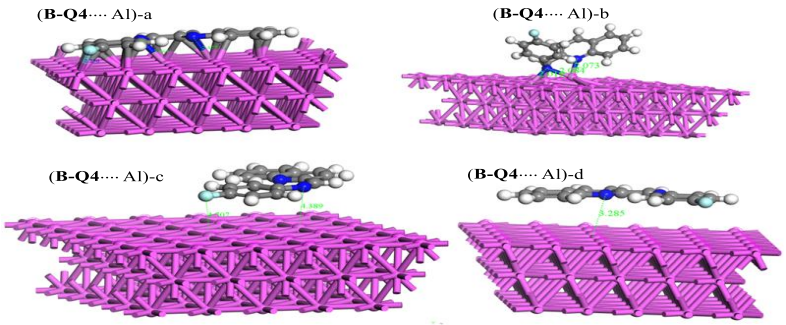

Figure 3: Different Adsorption Geometries Of B-Q4 Molecule On The Al(111) Surface And The Distance Between The Nearest Heteroatom To The Metal Surface

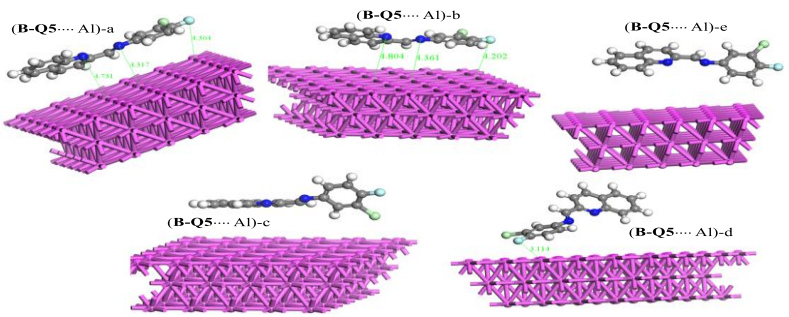

Figure 4: Different Adsorption Geometries of B-Q5 Molecule on the Al (111) Surface and the Distance between the Nearest Heteroatom to the Metal Surface

Table 3: Relative Energies (Kcal/Mol), Interaction Energies (Kcal/Mol), And Bond Distances Between Al (111) Surface and the Nearest Heteroatom Showing the Different Binding Sites of the Molecule on the Surface

Inhibitor	Configuration	E_{ads} (kcal/mol)	$E_{binding}$ (kcal/mol)	$\Delta E_{relative}$ (kcal/mol)	Bond distance (Å)
B-Q4	(**B-Q4**···Al)-a	-39.7314	39.7314	0	Al···F(2.256) Al···N(2.464) Al···N(2.477)
	(**B-Q4**·Al)-b	-39.7207	39.7207	0.0107	Al···N(2.049) Al···N(2.073)
	(**B-Q4**·Al)-c	-7.0254	7.0254	32.705	Al···N(4.707) Al···N(4.389)
	(**B-Q4**·Al)-d	-6.6540	6.6540	33.0774	Al···N(3.285)
B-Q5	(**B-Q5**·Al)-a	-9.1866	9.1866	0	Al···F(4.304) Al···N(4.317) Al···N(4.731)
	(**B-Q5**·Al)-b	-9.1421	9.1421	0.0445	Al···F(4.202) Al···N(4.804) Al···N(4.361)
	(**B-Q5**·Al)-c	-8.9224	8.9224	0.2642	-
	(**B-Q5**·Al)-d	-8.5327	8.5327	0.6539	Al···N(3.114)
	(**B-Q5**·Al)-e	-5.4228	5.4228	3.7638	-

DFT adsorption energies are per inhibitor molecule (gas phase)

Monte Carlo Simulation Studies

In addition to the gas-phase DFT adsorption calculations, Monte Carlo simulations were also carried out to further explore the adsorption properties of **B-Q4**, **B-Q5**, and protonated forms, **B-Q4H**, and **B-Q5H**, on Al(111) in simulated acidic aqueous environments. The sum of the adsorption energies, rigid adsorption energies, and deformation energies calculated from the simulations are presented in Table 4. It is worth noting that the adsorption energies in Table 4 are the total interaction energy of the whole simulation cell (including that of the inhibitor molecule, 80 water molecules, 10 H_3O^+ ions, and 10 Cl^- ions with the Al(111) surface); it is not per-molecule energies. Thus, the values cannot be compared directly regarding their magnitudes with the per-molecule gas-phase DFT adsorption energies reported in Table 3.

As revealed by the MC simulation results, all the forms of the inhibitors, both the neutral and protonated ones, have high negative total adsorption energy with respect to the simulated acidic environment, implying a high affinity and spontaneous adsorption process on the Al(111) surface. The adsorption configurations obtained after optimizing the simulations (Figure 5) show that the optimal adsorption configurations are achieved with both the inhibitors oriented almost parallel to the Al(111) surface, which means that there is a high surface coverage and an increased intermolecular contact between the inhibitor molecules and the metal surface. Such flat adsorption configurations are commonly associated with stronger adsorption interactions because they enable the π-electrons and heteroatoms of the inhibitor molecules to interact effectively with the metal surface atoms. Moreover, this near parallel orientation agrees with the DFT adsorption study, where the most stable orientations were also found to be horizontal, thereby demonstrating strong agreement between the two computational approaches.

The energy parameters calculated such as the total energy, adsorption energy, rigid adsorption energy and deformation energy give a quantitative understanding of the adsorption strength of the inhibitors on the aluminum surface. In adsorption simulations, a more negative adsorption energy indicates stronger interaction and greater stability of the adsorbed inhibitor–metal system. The results according to Table 4 show that the neutral inhibitors **B-Q4** and **B-Q5** exhibit adsorption energies of -1.52×10^3 kcal mol^{-1} and -1.50×10^3 kcal mol^{-1}, respectively. These highly negative values indicate strong spontaneous adsorption of both inhibitors onto the Al(111) surface, suggesting that the molecules can effectively form a protective layer that prevents aggressive species in the solution from reaching the metal surface.

Interestingly, the protonated species **B-Q4H** and **B-Q5H** exhibit even more negative adsorption energies of -1.56×10^3 kcal mol^{-1} and -1.58×10^3 kcal mol^{-1}, respectively. This shows that protonation increases the affinity of the inhibitor molecules in acidic media. This more intense adsorption of the protonated species could be explained by the electrostatic interactions between the positively charged molecules of the inhibitor and the negatively charged chloride ions in the solution that make it possible to form a more compact layer of adsorption on the metal surface. This type of behavior is often observed with corrosion inhibitors that are used in acidic chloride media, in which protonated inhibitor molecules synergistically interact with adsorbed chloride ions to cover the surface.

The same case can be found regarding the rigid adsorption energy, which is the interaction energy between the inhibitor and the metal surface and does not take into consideration the structural relaxation of the inhibitor molecule. The rigid adsorption energies for **B-Q4** and **B-Q5** are -1.56×10^3 kcal mol^{-1} and -1.53×10^3 kcal mol^{-1}, respectively, while those of the protonated species **B-Q4H** and **B-Q5H** are -1.59×10^3 kcal mol^{-1} and -1.61×10^3 kcal mol^{-1}. These results further confirm the stronger affinity of the protonated inhibitors toward the Al(111) surface. The slightly more negative rigid adsorption energy of **B-Q5H** suggests that this species exhibits the strongest adsorption interaction among the studied inhibitors. The values of the deformation energy (the structural energy penalty needed to ensure that the inhibitor molecule adapts to the surface during adsorption) ranges between about 31.57 to 34.03 kcal/mol across all systems. The deformation energies in the adsorption of organic corrosion inhibitors in the MC-based adsorption studies are quite small compared to the total adsorption energy (~1500 kcal/mol for the whole simulation cell), suggesting that the inhibitor molecules only slightly deform when adsorbing without disrupting the molecular framework. The range of deformation energies reported for similar adsorption studies of quinoline and Schiff base inhibitors on metal surfaces is

also comparable to that found in this study (Lgaz et al., 2016; Sithuba et al., 2024; Toghan et al., 2023 Kasprzhitskii & Lazorenko, 2021), consistent with the conclusion that the adsorption is thermodynamically favorable and does not require significant conformational reorganization.

Further insight into the interaction mechanism can be obtained from the energy contributions of the solvent and ionic species present in the simulation cell. The negative interaction energies observed for hydroxonium ions (H_3O^+), chloride ions (Cl^-), and water molecules indicate that these species interact with the inhibitor molecules and the metal surface, contributing to the stabilization of the adsorption system. In particular, the chloride ions show strong interaction energies, suggesting that they play an important role in mediating the adsorption process by forming electrostatic bridges between the positively charged protonated inhibitors and the metal surface. This effect is in agreement with the synergistic mechanism of adsorption in acidic chloride environments, which is widely reported. The optimized adsorption configurations presented in Figure 5 are yet another demonstration that the inhibitor molecules are located all over the Al(111) surface in a way that facilitates optimal surface coverage.

Table 4: The Monte Carlo Simulation Results Of B-Q4 and B-Q5 alongside Its Protonated Corrosion Inhibitor Materials on Al (111) Surface

	Total energy	Adsorption energy	Rigid adsorption energy	Deformation energy	hydoxium_opt : dEad/dNi	Chloride : dEad/dNi	q4-opt : dEad/dNi	water_opt : dEad/dNi
B-Q4	-1.56E+03	-1.52E+03	-1.56E+03	34.02610784	-106.4325526	-0.5909842	-103.0485579	-6.74978637
B-Q4H	-1.60E+03	-1.56E+03	-1.59E+03	33.30055954	-0.43357158	-101.2922002	-108.6826218	-7.42725891
B-Q5	-1.51E+03	-1.50E+03	-1.53E+03	31.56755041	-87.52650055	-0.51226188	-114.1472428	-6.95856802
B-Q5H	-1.59E+03	-1.58E+03	-1.61E+03	31.67474353	-1.27576453	-107.5169996	-120.7391386	-7.22463085

MC adsorption energies represent total simulation cell interaction energy (solvated system) and are not per-molecule values. They should not be directly compared in magnitude with the per-molecule gas-phase DFT adsorption energies in Table 3.

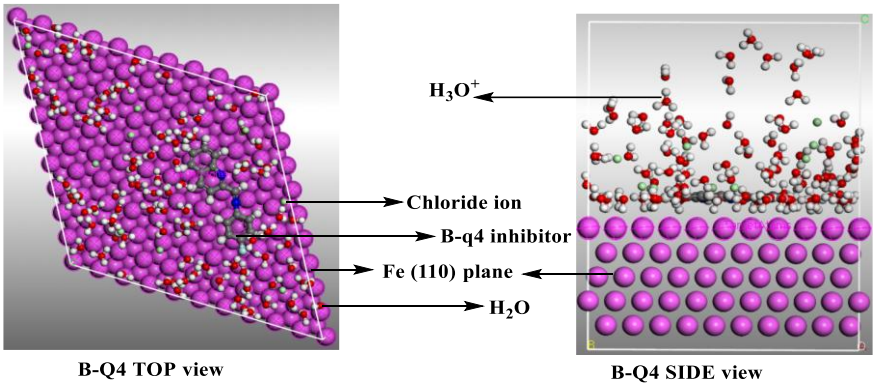

Figure 5a: Optimized Adsorption Configuration Of **B-Q4** Inhibitor On Al (111) Surface In The Presence Of Hcl (Solution Phase). Top and Side Views Illustrating the Interaction of Inhibitor with the Al Surface under Solvated Conditions, Including Water Molecules and Chloride Ions, Simulating A Corrosive Environment

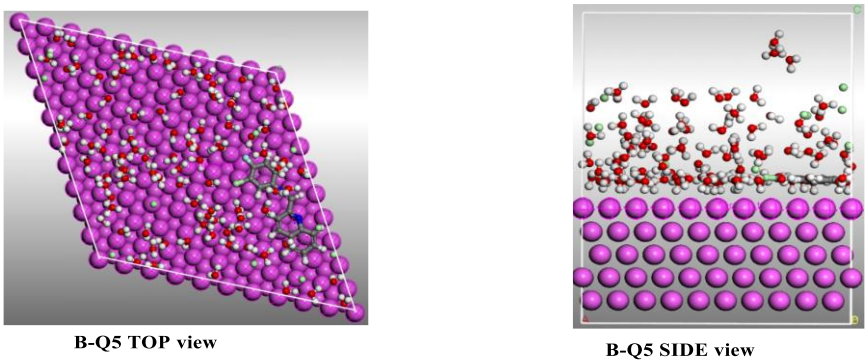

Figure 5b: Optimized Adsorption Configuration Of **B-Q5** Inhibitor On Al (111) Surface In The Presence Of Hcl (Solution Phase). Top and Side Views Illustrating the Interaction of Inhibitor with the Al Surface under Solvated Conditions, Including Water Molecules and Chloride Ions, Simulating A Corrosive Environment

The availability of water molecules, hydroxonium ions, and chloride ions in the simulation box resembles the corrosive HCl environment and how the inhibitor molecules compete with solvent molecules to occupy adsorption sites on the metal surface. This competition does not hinder the binding of the inhibitors on the surface, which indicates that the inhibitors have high affinities to aluminum.

Among all of the systems studied, the protonated **B-Q5H** inhibitor has the lowest adsorption energy and rigid adsorption energy values, which means that the adsorption interaction with the Al(111) surface is the strongest. This

suggests that **B-Q5H** is likely to provide the highest corrosion inhibition efficiency in acidic environments. The findings also indicate that the adsorption properties of the inhibitor molecules are improved by the protonation of these molecules, as it would be expected of organic inhibitors in highly acidic conditions. To sum up, the Monte Carlo simulation results demonstrate that both **B-Q4** and **B-Q5** inhibitors adsorb strongly on the Al(111) surface through a combination of electrostatic and molecular interactions. The adsorption energies are highly negative, the adsorption configurations are favorable and the interactions with chloride ions are cooperative and all these show that these inhibitors have the ability to form stable protective coatings over the aluminum surface, and reduce the accessibility of the corrosive species and improve corrosion resistance in acidic conditions.

It is worth noting that the Monte Carlo simulation results differ from that of the results from DFT adsorption studies which indicated that neutral **B-Q4** has a stronger intrinsic adsorption affinity in the gas phase. The reason for this is discussed in the next section. The simulations also illustrate the importance of the interactions between the adsorption layer and the surrounding solvent molecules, and with ions, such as the electrostatic and hydrogen bonding interactions between the chloride ions and the hydronium ions and the adsorption layer.

Comparison Between The DFT Studies And The Monte Carlo Study Analysis For The Adsorption Of The Inhibitor Under Study With Al (111) Surface

To obtain a comprehensive understanding of the adsorption mechanism of the investigated inhibitors on the aluminum surface, both Density Functional Theory (DFT) calculations and Monte Carlo (MC) simulations were employed. Although these two computational approaches operate at different theoretical levels, their results provide complementary insights into the interaction behavior of the inhibitors with the Al (111) surface. Table 5 summarizes the key findings from both approaches qualitatively, and illustrates the differences and similarities between the two methods.

Table 5: Qualitative Comparison of DFT and Monte Carlo Simulation Findings

Feature	DFT (Gas Phase, Neutral)	MC (Acidic Solvated, Neutral and Protonated)
Environment	Vacuum, no solvation	Explicit H_2O, H_3O^+, Cl^-
Inhibitor form	Neutral **B-Q4**, **B-Q5**	Neutral and protonated
Stronger adsorber	**B-Q4**	**B-Q5**H (protonated)
Adsorption type	Physisorption (intrinsic electronic)	Physisorption (electrostatic + dispersive)
Surface orientation	Horizontal and perpendicular	Near-parallel (maximizes coverage)
Adsorption spontaneity	Yes (negative E_{ads})	Yes (highly negative total energy)
Solvent role	Not included	Explicit; stabilizes adsorption layer
Energy basis	Per molecule (kcal/mol)	Total simulation cell (kcal/mol)

The DFT adsorption analysis focuses on the intrinsic electronic-level interactions between the neutral inhibitor molecules and the aluminum surface in the gas phase. The adsorption configurations of **B-Q4** and **B-Q5** on the Al(111) surface were analyzed through parameters such as adsorption energy, binding energy, relative energy, and bond distances between the heteroatoms of the inhibitor molecules and the aluminum atoms. The results showed that several adsorption configurations are possible, with the most stable arrangements characterized by very small relative energy differences. The calculated bond distances between aluminum atoms and heteroatoms such as nitrogen and fluorine indicate that these atoms serve as the primary interaction centers responsible for anchoring the inhibitor molecules onto the metal surface. The negative adsorption energies further confirm that the adsorption process is thermodynamically favorable and spontaneous. Among the configurations analyzed, **B-Q4** gave more negative adsorption energies than **B-Q5** in gas phase conditions, probably due to the stronger and more directional Al···F and Al···N interactions allowed by the mono-fluorine substituent in **B-Q4**, which are somewhat reduced in **B-Q5** by the steric effect of that additional chlorine. Thus, the DFT results provide detailed information about the intrinsic electronic interaction sites and the preferred binding configurations of the inhibitors on the aluminum surface under idealized vacuum conditions.

In contrast, the Monte Carlo simulations examine the adsorption process from a statistical and environmental, incorporating the effect of the acidic corrosion medium. Unlike the DFT approach, which typically evaluates isolated inhibitor–surface complexes in gas phase, the MC simulations include solvent molecules and aggressive ions such as chloride and hydroxonium ions to mimic the acidic corrosion environment. The total adsorption energies from MC simulations reflect the combined interaction energy of all the entire simulation cell and are not per molecule values. They should not be directly compared in magnitude with the gas-phase DFT adsorption energies in Table 3. The simulation results demonstrate that **B-Q4**, **B-Q5**, and their protonated forms (**B-Q4H** and **B-Q5H**) exhibit strong adsorption on the Al(111) surface with highly negative adsorption energies, indicating spontaneous and stable adsorption in the simulated acidic environment. The optimized configurations show that the inhibitor molecules tend to adopt nearly parallel orientations relative to the metal surface, thereby maximizing surface coverage and strengthening the interaction with the aluminum substrate, consistent with the horizontal adsorption geometries identified as most stable in the DFT study. Furthermore, the simulations highlight the role of the surrounding solvent molecules and ions in stabilizing the adsorption layer and influencing the adsorption configuration of the inhibitors. Under these solvated acidic conditions protonated **B-Q5**H has the highest total adsorption affinity among all species, which is due to stronger electrostatic interaction between protonated **B-Q5**H and the aluminum surface, as well as additional cooperative interaction with the chloride ions and simulation cell water molecules.

While **B-Q4** is the stronger adsorber in DFT, **B-Q5**H is the stronger adsorber in MC, reflecting the sensitivity of the adsorber behaviour to the molecular protonation state and simulation environment. Under gas-phase DFT conditions, neutral **B-Q4** benefits from more localized and directional electronic interactions with the Al(111) surface, as the mono-fluorine substituent promotes stronger Al···F and Al···N contacts without steric interference. However, taking the acidic aqueous environment in the MC simulations into account, both inhibitors are expected to be largely protonated, as the aqueous environment has a low pH. The protonation of

the inhibitor molecule results in a net positive charge and greatly increases electrostatic attraction to the aluminum surface and increases the cooperative interaction with neighboring ionic species. The electrostatic enhancements are more important for **B-Q5**H than for **B-Q4**H, probably due to the increased electron withdrawing effect of both the chlorine and the fluorine substituents in **B-Q5**H, leading to a more electropositive molecular framework that more strongly interacts with the surface environment in acidic conditions. Therefore, it is expected that protonated **B-Q5**H will have better adsorption affinity in real acidic corrosion conditions, while proton free **B-Q4** will show better intrinsic electronic interaction in idealized gas-phase conditions. Both results are valid and informative in the context of the two respective computational frameworks.

When considered together, the two computational approaches provide a coherent explanation of the inhibition mechanism. The DFT calculations identify the active adsorption centers and intrinsic electronic interactions responsible for inhibitor binding, while the Monte Carlo simulations demonstrate how these interactions translate into stable adsorption configurations under realistic corrosive conditions, where protonation state, solvation, and ionic environment collectively govern adsorption behavior. The agreement between the predicted interaction sites in the DFT analysis (based on N and F heteroatoms and the π-electron framework) and the near parallel adsorption positions found in MC simulations supports the idea that both the heteroatoms and the extended π-electron system are important in enabling the inhibitors to interact with the Al surface. The consistency between the findings obtained from these two methods strengthens the reliability of the computational predictions and supports the proposed mechanism by which **B-Q4** and **B-Q5** inhibit corrosion on the Al (111) surface in acidic environments.

CONCLUSION

This study employed an integrated density functional theory (DFT) and Monte Carlo simulation approach to investigate the adsorption behavior and corrosion inhibition potential of two quinoline-based Schiff base derivatives, **B-Q4** and **B-Q5**, on the Al(111) surface under simulated acidic media. Quantum chemical analyses reveal strong π-electron delocalization and significant donor–acceptor interactions within both molecules, indicating good electron-donating ability and favorable electronic characteristics for adsorption on metal surfaces. NCI and QTAIM analyses further show that weak dispersive interactions dominate the intramolecular interaction patterns of the isolated inhibitor molecules, providing electronic context for the physisorptive adsorption mechanism observed in the adsorption calculations.

The gas-phase DFT adsorption studies demonstrate that both inhibitors interact spontaneously with the aluminum surface, as confirmed by negative adsorption energies and favorable adsorption geometries. Among the configurations analyzed, **B-Q4** exhibits stronger adsorption energies than **B-Q5**, attributed to the stronger and more directional Al···F and Al···N interactions facilitated by the mono-fluorine substituent, which are partially disrupted in **B-Q5** by the additional chlorine atom. The inhibitors preferentially adopt horizontal orientations on the Al(111) surface, which enhances surface coverage and strengthens inhibitor–metal interactions. In support of the topological analyses, the resulted adsorption energies for **B-Q4** and **B-Q5** inhibitors are below the magnitude of -100 kcal/mol, consistent with a physisorption mechanism. The dispersive character of the NCI intermolecular interactions, the NBO analysis indicative of electron density localization on the nitrogen and halogen centers, and the charge distribution analysis reported in our earlier work (Oladipo et al., 2025) are all suggestive that both inhibitors have the electronic character of physisorbing molecules, interacting with metal surfaces by weak, delocalized contacts, but not by bond formation.

Monte Carlo simulations conducted under realistic acidic conditions (incorporating explicit water molecules, hydronium ions, and chloride ions) further confirm the strong adsorption affinity of the inhibitors for the Al (111) surface. Protonation of the inhibitors enhances their adsorption strength, with the protonated species **B-Q5H** demonstrating the strongest total adsorption affinity under solvated conditions due to enhanced electrostatic interactions.

This result is in contrast to the gas-phase DFT result, where the intrinsic adsorption of neutral **B-Q4** is stronger as opposed to the electrostatic and cooperative solvation effect in an explicit acidic solvent performed in Monte Carlo simulation. Both results are consistent in their own computational methods and the combined result gives a complete picture of the adsorption mechanism. Therefore, the combined computational results demonstrate that **B-Q4** and **B-Q5** are promising corrosion inhibitors for aluminum in hydrochloric acid environments. Their adsorption is primarily governed by physisorption through dispersive and electrostatic interactions, enabling the formation of a protective adsorbed film that limits access of corrosive species to the metal surface.

Despite these conclusions, there are some limitation in this research study. The DFT adsorption calculation was done without explicit solvation, the NCI and QTAIM analyses were carried out on the free inhibitor molecules and not the adsorption complexes, and the COMPASS force field employed in MC simulations contains classical approximations that do not necessarily reflect quantum mechanical effects like charge transfer and polarization at the inhibitor–surface interface. Most importantly, this work is a predictive computational study, which has not been validated experimentally by electrochemical or surface analytical methods on actual aluminum in HCl for these specific inhibitors; therefore, the results are theoretical values of inhibition potentials and conclusions drawn from this work can only be tentative until experimental validation has been performed. Experimental validation using electrochemical methods (such as potentiodynamic polarization and electrochemical impedance spectroscopy) and surface analytical techniques (scanning electron microscopy, AFM and XPS) should be done in the future to confirm the predicted adsorption behavior and inhibition efficiency of **B-Q4** and **B-Q5** on the surface of aluminum in acidic solutions. The periodic slab calculations with dispersion corrections (DFT-D3) and the application of molecular dynamics simulations at finite temperature would make the prediction of the adsorption more reliable and dynamic.

REFERENCES

Ahmed, M. A., Amin, S., & Mohamed, A. A. (2024). Current and emerging trends of inorganic, organic and eco-friendly corrosion inhibitors. RSC Advances, 14(43), 31877–31920.

Aljibori, H., Alamiery, A., & Kadhum, A. (2023). Advances in corrosion protection coatings: A comprehensive review. Int. J. Corros. Scale Inhib, 12(4), 1476–1520.

Alqarni, N., El-Gammal, B., Fawzy, A., Bahir, A. A., & Toghan, A. (2022). Investigation of Expired Ticarcillin and Carbenicillin Drugs for Inhibition of Aluminum Corrosion in

Hydrochloric Acid Solution. International Journal of Electrochemical Science, 17(12), 2212113. https://doi.org/10.20964/2022.12.99

Andersson, M. P., & Uvdal, P. (2005). New Scale Factors for Harmonic Vibrational Frequencies Using the B3LYP Density Functional Method with the Triple-ζ Basis Set 6-311+G(d,p). The Journal of Physical Chemistry A, 109(12), 2937–2941. https://doi.org/10.1021/jp045733a

Andrienko, G. (2010). Chemcraft-graphical software for visualization of quantum chemistry computations. See Https://Www. Chemcraftprog. Com.

Aslam, R., Mobin, M., Zehra, S., & Aslam, J. (2022). A comprehensive review of corrosion inhibitors employed to mitigate stainless steel corrosion in different environments. Journal of Molecular Liquids, 364, 119992.

Avdeev, Y. G., & Kuznetsov, Y. I. (2022). Acid corrosion of metals and its inhibition. A critical review of the current problem state. International Journal of Corrosion and Scale Inhibition, 11(1), 111–141.

Aydın, F. (2023). A review of recent developments in the corrosion performance of aluminium matrix composites. Journal of Alloys and Compounds, 949, 169508.

Azeez, Y. H., Mamand, D. M., Omer, R. A., Awla, A. H., & Omar, K. A. (2024). Investigation of corrosion inhibition and adsorption properties of quinoxaline derivatives on metal surfaces through DFT and Monte Carlo simulations. Corrosion Reviews, 42(6), 775-793. https://doi.org/10.1515/corrrev-2024-0007.

Badeji, A. A., Pathmanathan, K., Abdullah, H. Y., Hossain, I., & Runde, M. (2025). Unveiling the catalytic versatility of transition metal-doped coal char systems for hydrogen evolution reaction: A first-principles approach. Chemical Physics, 599, 112882. https://doi.org/10.1016/j.chemphys.2025.112882

Bader, R. F. (1985). Atoms in molecules. Accounts of Chemical Research, 18(1), 9–15.

Bedair, M. A., Abuelela, A. M., Alshareef, M., Owda, M., & Eliwa, E. M. (2023). Ethyl ester/acyl hydrazide-based aromatic sulfonamides: facile synthesis, structural characterization, electrochemical measurements and theoretical studies as effective corrosion inhibitors for mild steel in 1.0 M HCl. RSC advances, 13(1), 186-211. https://doi.org/10.1039/d2ra05939h.

Bender, R., Féron, D., Mills, D., Ritter, S., Bäßler, R., Bettge, D., De Graeve, I., Dugstad, A., Grassini, S., & Hack, T. (2022). Corrosion challenges towards a sustainable society. Materials and Corrosion, 73(11), 1730–1751.

Birbilis, N., & Hinton, B. (2011). Corrosion and corrosion protection of aluminium. Fundamentals of Aluminium Metallurgy, 574–604.

Chen, L., Lu, D., & Zhang, Y. (2022). Organic compounds as corrosion inhibitors for carbon steel in HCl solution: A comprehensive review. Materials, 15(6), 2023.

Dennington, R., Keith, T., & Millam, J. (2023). GaussView, Version 6.0. 1.6, Semichem Inc., Shawnee Mission, KS, 2016.

Dutta, D., Dutta, P., & Chutia, G. P. (2026). Electron delocalization as a design principle in functional materials: From molecular structure to macroscopic properties. Structural Chemistry, 1-28. https://doi.org/10.1007/s11224-026-02769-7

Farag, A. A., Tawfik, S. M., Abd-Elaal, A. A., & Abdelshafi, N. (2024). Detailed DFT/MD simulation, QSAR modeling, electrochemical, and surface morphological studies of self-assembled surfactants as eco-friendly corrosion inhibitors for copper in 1 M HNO3 solution. Journal of Industrial and Engineering Chemistry, 138, 237–255.

Frisch, M., Trucks, G., Schlegel, H., Scuseria, G., Robb, M., Cheeseman, J., Scalmani, G., Barone, V., Petersson, G., & Nakatsuji, H. (2016). Gaussian 16 Revision C. 01, 2016. Gaussian Inc. Wallingford CT, 1, 572.

Gabryelczyk, A., Ivanov, S., Bund, A., & Lota, G. (2021). Corrosion of aluminium current collector in lithium-ion batteries: A review. Journal of Energy Storage, 43, 103226.

Galvez, C. E., Piro, O. E., Echeverría, G. A., Vignesh, K., Thamotharan, S., Loandos, M. D. H., & Gil, D. M. (2025). Supramolecular assembly mediated by hydrogen bonds and weak noncovalent interactions in two eucalyptol derivatives with potential antineoplastic activity: Crystal structure, Hirshfeld surface analysis, DFT calculations and molecular docking analysis. CrystEngComm, 27(22), 3806–3822. https://doi.org/10.1039/D5CE00308C

Gervasio, G., Bianchi, R., & Marabello, D. (2004). About the topological classification of the metal–metal bond. Chemical Physics Letters, 387(4–6), 481–484.

Humphrey, W., Dalke, A., & Schulten, K. (1996). VMD: Visual molecular dynamics. Journal of Molecular Graphics, 14(1), 33–38. https://doi.org/10.1016/0263-7855(96)00018-5

Ibeji, C. U., Akintayo, D. C., Oluwasola, H. O., Akintemi, E. O., Onwukwe, O. G., & Eziomume, O. M. (2023). Synthesis, experimental and computational studies on the anti-corrosion performance of substituted Schiff bases of 2-methoxybenzaldehyde for mild steel in HCl medium. Scientific Reports, 13(1), 3265. https://doi.org/10.1038/s41598-023-30396-3.

Ikeuba, A. I., Njoku, C. N., Ekerenam, O. O., Njoku, D. I., Udoh, I. I., Daniel, E. F., Uzoma, P. C., Etim, I.-I. N., & Okonkwo, B. O. (2024). A review of the electrochemical and galvanic corrosion behavior of important intermetallic compounds in the context of aluminum alloys. RSC Advances, 14(43), 31921–31953.

Kania, H. (2023). Corrosion and anticorrosion of alloys/metals: The important global issue. Coatings, 13(2), 216.

Kasprzhitskii, A., & Lazorenko, G. (2021). Corrosion inhibition properties of small peptides: DFT and Monte Carlo simulation studies. Journal of Molecular Liquids, 331, 115782.

Kumar, P., Holmberg, K., Soni, I., Islam, N., Kumar, M., Shandilya, P., Sillanpää, M., & Chauhan, V. (2024). Advancements in ionic liquid-based corrosion inhibitors for sustainable protection strategies: From experimental to computational insights. Advances in Colloid and Interface Science, 333, 103303.

Lgaz, H., Salghi, R., Jodeh, S., Ramli, Y., Larouj, M., Toumiat, K., Quraishi, M.A., Oudda, H., & Jodeh, W. (2016). Understanding the adsorption of quinoxaline derivatives as corrosion inhibitors for mild steel in acidic medium: Experimental, theoretical and molecular dynamic simulation studies. Journal of Steel Structures & Construction, 2(1), 2472-0437. https://doi.org/10.4172/2472-0437.1000111

Louis, H., Ifediora, L. P., Enudi, O. C., Unimuke, T. O., Asogwa, F. C., & Moshood, Y. L. (2021). Evaluation of the excited state dynamics, photophysical properties, and the influence of donor substitution in a donor-$$\pi$$-acceptor system. Journal of Molecular Modeling, 27(10), 284. https://doi.org/10.1007/s00894-021-04875-1

Lu, T. (2025). Visualization analysis of covalent and noncovalent interactions in real space. Angewandte Chemie International Edition, 64(29), e202504895.

Ma, C., Gong, L., Zhang, X., & Liu, H. (2023). Investigation of linear and second-order nonlinear optical properties of donor-acceptor interaction derivatives based on acceptor DCPPr core. Journal of Molecular Structure, 1282, 135203. https://doi.org/10.1016/j.molstruc.2023.135203

McCafferty, E. (2010). Corrosion Inhibitors. In: Introduction to Corrosion Science. Springer, New York, NY. https://doi.org/10.1007/978-1-4419-0455-3_12

Meunier, M., & Robertson, S. (2021). Materials Studio 20th anniversary. Molecular Simulation, 47(7), 537–539. https://doi.org/10.1080/08927022.2021.1892093

Odozi, N., Festus, C., & Sorbari, K. (2022). Adsorption and anticorrosion properties of mild-steel treated 2-[(3-hydroxylpyridin-2-yl) amino] naphthalene-1, 4-Dione Schiff base in 1m-HCl solution: Synthesis, experimental and computational studies. Fudma Journal of Sciences, 6(2), 144-155.

Oladipo, S. D., Luckay, R. C., Olalekan, S. O., Badeji, A. A., Matinise, N., & Tshikhudo, F. (2025). Investigating the Inhibitory Potential of Halogenated Quinoline Derivatives against MAO-A and MAO-B: Synthesis, Crystal Structure, Density Functional Theory, and Molecular Dynamics Simulations. ACS Omega, 10(25), 26500–26519. https://doi.org/10.1021/acsomega.4c11530

Pal, R., Patra, S. G., & Chattaraj, P. K. (2022). Can a chemical bond be exclusively covalent or ionic? Journal of Chemical Sciences, 134(4), 108.

Pietschmann, J. (2023). Surface pretreatment of metals. In Industrial powder coating: Basics, Methods, Practical Application (pp. 209–275). Springer.

Reed, A. E., Curtiss, L. A., & Weinhold, F. (1988). Intermolecular interactions from a natural bond orbital, donor-acceptor viewpoint. Chemical Reviews, 88(6), 899-926. https://doi.org/10.1021/cr00088a005.

Saravanan, K. G., Kirubaharan, A. K., & Vishwakarma, V. (2021). Introduction to Surface Coatings. In Polymetallic Coatings to Control Biofouling in Pipelines (pp. 53–76). CRC Press.

Shahini, M., Ramezanzadeh, M., Bahlakeh, G., & Ramezanzadeh, B. (2021). Superior inhibition action of the Mish Gush (MG) leaves extract toward mild steel corrosion in HCl solution: Theoretical and electrochemical studies. Journal of Molecular Liquids, 332, 115876.

Sithuba, T., Kabanda, M. M., Madala, N. E., & Murulana, L. C. (2024). Exploration of UV-induced geometrical isomer-enriched Helichrysum kraussii extract as a corrosion inhibitor for Al(111) surface in 1.0 M hydrochloric acid: An experimental and theoretical study. Results in Surfaces and Interfaces, 16, 100268. https://doi.org/10.1016/j.rsurfi.2024.100268

Suvitha, A., Venkataramanan, N. S., Sahara, R., & Kawazoe, Y. (2019). A theoretical exploration of the intermolecular interactions between resveratrol and water: A DFT and AIM analysis. Journal of Molecular Modeling, 25(3), 56. https://doi.org/10.1007/s00894-019-3941-7

Toghan, A., Fawzy, A., Alakhras, A. I., Alqarni, N., Zaki, M. E. A., Sanad, M. M. S., & Farag, A. A. (2023). Experimental Exploration, RSM Modeling, and DFT/MD Simulations of the Anticorrosion Performance of Naturally Occurring Amygdalin and Raffinose for Aluminum in NaOH Solution. Coatings, 13(4), 704. https://doi.org/10.3390/coatings13040704

Uzah, T. (2024). DFT and monte carlo simulation for the prediction of corrosion inhibitive efficacy of selected thiosemicarbazide derivatives on Al 111) and Cu 111) surfaces in acidic media. Journal of Medicinal and Nanomaterials Chemistry, 6(1). https://doi.org/10.48309/jmnc.2024.1.7

Vernack, E., Costa, D., Tingaut, P., & Marcus, P. (2020). DFT studies of 2-mercaptobenzothiazole and 2-mercaptobenzimidazole as corrosion inhibitors for copper. Corrosion Science, 174, 108840. https://doi.org/10.1016/j.corsci.2020.108840

Wang, L. K., & Wang, M.-H. S. (2025). Environmental management of electroplating and metal-finishing operations. In Control of heavy metals in the environment (pp. 325–378). CRC Press.

Xhanari, K., Finšgar, M., Hrnčič, M. K., Maver, U., Knez, Ž, & Seiti, B. (2017). Green corrosion inhibitors for aluminium and its alloys: A review. RSC Advances, 7(44), 27299–27330.

Xu, X. T., Xu, H. W., Li, W., Wang, Y., & Zhang, X. Y. (2022). A combined quantum chemical, molcular dynamics and Monto Carlo study of three amino acids as corroison inhibitors for aluminum in NaCl solution. Journal of Molecular Liquids, 345, 117010. https://doi.org/10.1016/j.molliq.2021.117010

Zamindar, S., Mandal, S., Murmu, M., & Banerjee, P. (2024). Unveiling the future of steel corrosion inhibition: A revolutionary sustainable odyssey with a special emphasis on N+ -containing ionic liquids through cutting-edge innovations. Materials Advances, 5(11), 4563–4600. https://doi.org/10.1039/D4MA00156G

Zehra, S., Mobin, M., & Aslam, J. (2022). An overview of the corrosion chemistry. Environmentally Sustainable Corrosion Inhibitors, 3–23.

Zhan, J., Lei, Z., & Zhang, Y. (2022). Non-covalent interactions of graphene surface: Mechanisms and applications. Chem, 8(4), 947–979.

Zhang, I. Y., Wu, J., & Xu, X. (2010). Extending the reliability and applicability of B3LYP. Chemical Communications, 46(18), 3057. https://doi.org/10.1039/c000677g